



A processable high thermal conductivity epoxy composites with multi-scale particles for high-frequency electrical insulation

Yan-Hui Song¹ · Li-Juan Yin¹ · Shao-Long Zhong¹ · Qi-Kun Feng¹ · Haidong Wang² · Pinjia Zhang¹ · Hai-Ping Xu³ · Tong Liang⁴ · Zhi-Min Dang¹

Received: 20 December 2023 / Revised: 12 May 2024 / Accepted: 5 June 2024 / Published online: 2 July 2024
© The Author(s) 2024

Abstract

The solid-state transformer (SST) in the renewable energy grid is developing in the way of high voltage and high frequency, which often results in a sharp increase in heat production of the equipment and accelerates the failure of the insulating materials. Epoxy resin (EPR) is commonly used as an insulation material for SST due to its excellent electrical insulating properties, processing performance (viscosity), and low price. However, the thermal conductivity of EPR is only about 0.2 W/(m·K), which leads to poor insulating performance under high frequency and temperature. To enhance thermal conductivity, a substantial quantity of highly thermally conductive particles is incorporated into the EPR, accompanied by a severe increase in electrical insulation defects and viscosity. This study utilized a multi-scale particle-filled approach to investigate the thermal conductivity, processing characteristics, and high-frequency electrical insulation performance of composites. The composite, filled with 25 μm BN and 5 μm SiO₂ particles, enhances thermal conductivity to 0.732 W/(m·K) and demonstrates superior electrical insulating properties at both 10 kHz and 20 kHz bipolar square waves (with an increase of 131.76% and 163.97% in relative EPR, respectively), as well as good processability. Meanwhile, it is found that the dielectric loss, thermal conductivity, and electric field distribution of the composite are the main factors affecting the electrical insulating properties from 10 to 20 kHz under high voltage.

Keywords Epoxy composites · High frequency · Electrical insulating property · Thermal conductivity · Viscosity

1 Introduction

Solid-state transformer (SST), which combine power electronics technology to achieve electric power regulation, electrical isolation, voltage level conversion, and other functions, are suitable for renewable energy power generation grid connection [1–3]. In addition, SST is widely used in electric locomotives, car charging stations, and data centers [4, 5]. However, studies have shown that the breakdown strength of electrical insulation materials used in SST with a working frequency range from hundreds of Hz to tens of kHz is significantly lower than that of traditional electrical insulation conditions (DC, AC) [6, 7]. Most researchers believe the unfavorable thermal conductivity and dielectric loss of electrical insulating materials under high frequency and high voltage cause temperature accumulation (up to 100 °C) within the SST, resulting in rapid insulation failure [8, 9]. Therefore, the large-scale applications of SST urgently require materials with high heat dissipation and excellent high-frequency electrical insulating properties.

✉ Li-Juan Yin
yinlj2022@tsinghua.edu.cn
✉ Zhi-Min Dang
dangzm@tsinghua.edu.cn

¹ Department of Electrical Engineering, State Key Laboratory of Power System Operation and Control, Tsinghua University, Beijing 100084, China

² Department of Engineering Mechanics, Key Laboratory for Thermal Science and Power Engineering of Ministry of Education, Tsinghua University, Beijing 100084, China

³ Shanghai Engineering Research Center of Advanced Thermal Functional Materials, Shanghai Polytechnic University, Shanghai 201209, China

⁴ State Key Laboratory of Information Photonics and Optical Communications, School of Science, Beijing University of Posts and Telecommunications, Beijing 100876, China

Compared with the gaseous (SF_6) and liquid (transformer oil) insulating dielectrics, epoxy resin (EPR) as a solid insulating dielectric possesses inherent advantages of a mature preparation process, low cost, and excellent electrical insulating performance, which greatly reduces the volume of the SST [10–12]. However, the thermal conductivity of epoxy resin is only about $0.2 \text{ W}/(\text{m}\cdot\text{K})$, which is far less than that of conductor materials and magnetic materials in SST, posing a significant threat to the safety and reliability of SST working at high frequencies and high voltages [10]. To address the low thermal conductivity of epoxy resin, many strategies have been investigated, such as introducing high thermal conductivity fillers or liquid crystal groups in the polymer matrix [13, 14], optimizing the interface between fillers and matrix [15–17], and designing ingenious three-dimensional thermal conductive networks [18, 19]. Among all the ways, adding high thermally conductive fillers to improve the thermal conductivity of polymer matrix is the most promising approach for large-scale industrial production. Moreover, compared with conductive fillers such as metal or carbon materials, the polymer composites with thermally conductive ceramics fillers such as alumina (Al_2O_3), aluminum nitride (AlN), and boron nitride (BN) have good electrical insulating properties which are more suitable for high-voltage power equipment [20–23]. In addition, the processing performance (viscosity) of epoxy resin composites in the uncured state is also necessary for large-scale industrial applications [24, 25]. The small size, irregular shape, and high filling content of fillers lead to a rapid increase in the viscosity of EPR composites [26–29]. Particularly, considering the impact of particle spacing and mutual friction within the polymer matrix, it has been found that the respective compound systems of spherical alumina (Al_2O_3) and spherical aluminum (Al) with optimized particle size distribution can reduce the viscosity of EPR composites, even though the particle filling amount is up to 50 vol% [30, 31]. Nevertheless, in the case of high-quality interconnection networks, point-to-point connections between spherical fillers result in low heat transfer efficiency within the composite due to insufficient interfacial overlap areas [25, 32]. Therefore, the appropriate addition of one-dimensional or two-dimensional fillers in the design of the compound system can improve the heat transfer efficiency and ensure better processing performance.

To evaluate the electrical insulating properties of polymer composites, high-voltage tests, including breakdown strength, breakdown time, and DC conductivity are the most critical [33–38]. However, the electrical insulation test of epoxy-based thermally conductive and electrical insulating materials was usually tested at low frequency in previous researches [35, 39, 40]. In the high-frequency and high-voltage fields, few researchers have carried out different frequency breakdown strength or breakdown time tests

[36, 37, 41]. For instance, Yao et al. observed a substantial rise in material temperature as the frequency [36]. At a frequency of 20 kHz, the test sample with a thermal conductivity of $0.825 \text{ W}/(\text{m}\cdot\text{K})$ exhibited the largest breakdown time, whereas at a frequency of 44 kHz, the test sample with the highest thermal conductivity of $1.19 \text{ W}/(\text{m}\cdot\text{K})$ exhibited the longest breakdown time. Awais et al. prepared EPR composites based on $0.5 \mu\text{m}$ BN and 50 nm $\text{TiO}_2@\text{SiO}_2$ and measured the breakdown strength of 5 kHz and 10 kHz at different temperatures [37]. The results indicated that EPR composites with 5.0 wt% BN and 3.0 wt% $\text{TiO}_2@\text{SiO}_2$ showed the best high-frequency breakdown strength and thermal conductivity of $0.45 \text{ W}/(\text{m}\cdot\text{K})$. Therefore, it would be inferred that the high-frequency electrical insulating performance does not directly exhibit a strong correlation with the thermal conductivity of the materials. Besides, due to the researchers used self-made power supplies, the output waveforms were not standard, and the test data were incomparability, resulting in many present results showed the contradictory viewpoints [41–43]. The breakdown mechanism of the dielectrics and how to simultaneously improve its thermal conductivity and electrical insulating properties at high frequency still remain to be studied.

Due to these thorny problems, we designed a series of EPR composites filled with multi-scale fillers based on a large fraction of spherical particles and a small fraction of two-dimensional sheets to improve overall performance. Since the EPR composites are often used in high-voltage and high-frequency fields, the BN (5.9 eV, $29 \sim 300 \text{ W}/(\text{m}\cdot\text{K})$), SiO_2 (9 eV, $1.5 \text{ W}/(\text{m}\cdot\text{K})$) and Al_2O_3 (7.2 ~ 8.8 eV, $38 \sim 42 \text{ W}/(\text{m}\cdot\text{K})$) particles with good electrical insulating properties and high thermal conductivity are selected as fillers [44–47]. In this study, spherical particles (different combinations of $5 \mu\text{m}$ SiO_2 or $40 \mu\text{m}$ Al_2O_3) were used as the primary part of the thermal conductive network of the EPR composites. A small amount of BN sheets was filled to increase the contact area between the spherical particles in the matrix, which significantly improved the thermal conductivity of the composites, and helped to maintain the viscosity of the uncured composites at a low level. Additionally, the output waveform of the high-frequency power supply adopted in this work is a bipolar square wave, consistent with Zhao et al., which is similar to the actual working condition of SST [7]. For the multi-scale particle-filled systems with different particles at a content of 50 wt%, the morphologies were observed by scanning electron microscopy (SEM), and the thermal characteristics of the materials were tested by thermogravimetric analysis (TGA), differential scanning calorimetry (DSC), and thermal conductivity test. The viscosity, electrical insulating properties at high frequencies, dielectric properties, and temperature rise of the EPR composites were also evaluated. This study provides the theoretical basis and new idea for the design of high-voltage and high-frequency insulating materials applied in the SST.

2 Experimental

2.1 Materials

The epoxy resin (EPR) used in the work was bisphenol A diglycidyl ester (E51) with an epoxy value of approximately 0.51 mol/100 g, which was provided by Nantong Xingchen Synthetic Material Co., Ltd. (Nantong, China). The curing agent, methyl hexahydrophthalic anhydride (MeHHPA), was supplied by Guangzhou Kuibang Chemical Co., Ltd. (Guangzhou, China), and the accelerator 2,4,6-tri(dimethylaminomethyl)phenol (DMP-30) was provided from Jiangsu Dandelion New Materials Co., Ltd. (Jiangsu China). The three different inorganic ceramic particles used in this work include SiO_2 (average diameter was 5 μm), BN (average in-plane diameter was 25 μm), Al_2O_3 (average diameter was 40 μm), which were purchased from Ningbo Jinlei Nanomaterials Technology Co., Ltd. (Ningbo, China), Ningbo Bohuas Nanotechnology Co., Ltd. (Ningbo, China), and Ya'an Baitu High-tech Materials Co., Ltd. (Ya'an, China), respectively.

2.2 Preparation of EPR composites

The specific preparation process of the EPR composites is shown in Fig. 1a. At first, the epoxy precursor was obtained by homogeneously mixing the polymer matrix (E51), the curing agent (MeHHPA), and accelerator (DMP-30) with a fixed weight ratio (100/86/0.1) by the planetary stirrer. The planetary stirrer operates under vacuum which reduces the large number of air bubbles generated by mechanical stirring [31]. Subsequently, the fillers were added to the epoxy precursor, which the planetary stirrer continued mixing and degassing. The single stirring process was 900 rpm (60 s), 2000 rpm (120 s), 1500 rpm (60 s), and the total stirring was three times. In particular, the pure epoxy precursor was stirred once and twice with fillers. The mixture was then poured into the molds and placed in heat press and oven for curing. It was pre-cured at 100 °C and 2 MPa for 1 h, post-cured at 120 °C for 1 h, and 150 °C for 6 h, eventually obtaining the EPR composites after slowly decreasing to room temperature [30, 36].

2.3 Characterization

The morphologies of SiO_2 , BN, Al_2O_3 particles, and the EPR composites were observed by using a scanning electron microscope (SEM, Hitachi S-5500). The elemental composition and distribution of the EPR composites were analyzed by an energy-dispersive spectrometer (EDS, Hitachi S-5500). The particle size distribution of SiO_2 , BN, and Al_2O_3 was obtained by a laser granularity analyzer

(Mastersizer3000, Malvern). Automatic True Densitometer (AccuPycII 1340, micromeritics) was utilized to test the densities of SiO_2 , BN, and Al_2O_3 particles. The rheological behavior (viscosity) of EPR composites at 25 °C and 65 °C with angular frequency from 1 to 100 rad/s was tested by a rheometer (MCR-301, Anton Paar, Germany).

Thermogravimetric analysis (TGA) of EPR composites was carried out by a thermal analyzer (SDT Q600, TA Instruments, USA) at a 20 °C/min heating rate from 25 to 800 °C under a nitrogen atmosphere. The glass transition temperature (T_g) and specific heat capacity $C(T)$ were measured by the differential scanning calorimeter (DSC250, TA Instruments, USA). The T_g and $C(T)$ were tested in the temperature range of 20 to 200 °C with a heating rate of 10 °C/min and 10 to 50 °C with a heating rate of 5 °C/min, respectively. The laser thermal conductivity analyzer (LFA467, NETSCH, Germany) was used to test the thermal diffusivity of the EPR composites at 25 °C. The thermal conductivity $\lambda(T)$ of EPR composites was calculated by Eq. (1) [48], where $\alpha(T)$, $\rho(T)$, and $C(T)$ are the thermal diffusivity, density, and specific heat capacity of the composites, respectively.

$$\lambda(T) = \alpha(T)\rho(T)C(T) \quad (1)$$

The wide spectrum analyzer (Novocontrol Concept 40, Novocontrol Technology, Germany) was utilized to acquire the dielectric properties of EPR composites in the frequency range from 10^0 to 10^6 Hz under 20 to 200 °C.

The HVJB transformer of Suzhou HaiWo Technology Co., Ltd. (Suzhou, China) could output the voltage to 150 kV. The voltage output controller of Wuhan Torch Electromechanical Instrument Co., Ltd. (Wuhan, China) was used to test the breakdown strength of EPR composites at 50 Hz under room temperature with a consistent voltage rise of 1 kV/s, according to the IEC 60243-1:2013 standard. The high-frequency breakdown time measurement of EPR composites was based on the High-Frequency Bipolar Square Wave Power Supply test system (AIYS-20 kV) of Tianjin MingRuiChuang Technology Co., Ltd. (Tianjin, China), which could output ± 20 kV voltage and the rising edge of the square waveform was about 10 μs [16, 36, 42]. Herein, the test voltage amplitude was set as ± 17.5 kV, and the frequency was measured at 10 kHz and 20 kHz. In order to avoid flashover, the ball-to-ball electrodes with a diameter of 20 mm and the test samples were dipped in silicone oil. The Weibull distribution was used for data analysis, and each sample was tested 15 times. Meanwhile, the high-frequency electric-to-heating experiments were carried out with a hemispherical-to-hemispherical electrode diameter of 25 mm, and the temperature rise of the samples was observed by a thermal infrared imager tix580 (Fluke, USA), which was replicated five times for each

composite in the test. The DC conductivity characteristics of EPR composites were measured using a test rig consisting of a high precision high voltage DC power supply (Keithley 2635B, USA), a high precision microcurrent meter (Keithley 2290–10, USA), and a three-electrode system. In particular, the measured electric strength was 10 kV/mm, and the measurement temperature ranged from 25 to 200 °C. The isothermal surface potential decay (ISPD) experiment was used to obtain the trap energy levels and densities of carriers. The ISPD setup consisted of a high-voltage DC power supply, a data collection device, and a needle-plate electrode system. The distance from the needle electrode to the sample was 5 mm. The corona charging voltage was –5 kV, and the charging time was 60 s. The Trek 347 was used to collect the depolarization data for 600 s. The sample thickness was 500 μm for all the high-voltage tests with a thickness error below 10%.

The Young's modulus of EPR composites was tested by a universal material tensile machine (Instron 3343, Instron, UK) using a dumbbell-shaped mold to prepare the sample for uniaxial tensile test. The thickness of the sample is 0.5 mm, and the stretching area is 12 mm × 2 mm with stretching at a rate of 2 mm/min. Young's modulus is determined by taking the slope of the tangent line at 5% of the deformation.

3 Results

3.1 Design for multi-scale particle compound system

For the inorganic particle compound system, the physical characteristics, shape, size, and filling ratio of the particles play a decisive role in the various properties of the composites. Generally, inorganic particles with small size and large size are beneficial to improve electrical insulating performance and thermal conductivity, respectively [37, 41]. The filling ratio of different particles will directly affect the processing performance of the composites, causing high viscosity, for example, which is unsuitable for enhancing thermal conductivity and electrical insulating properties. In conjunction with the previous section, 5 μm SiO₂, 25 μm BN, 5 μm Al₂O₃, and 40 μm Al₂O₃ were selected as fillers.

Herein, a three-particle filling system was compared with three two-particle filling systems. The three-particle system was designed using the Dinger-Funk model, as one of the widely used particle packing theories, which can be expressed as follows [30, 31]:

$$U(D_p) = 100 \frac{D_p^n - D_{\min}^n}{D_{\max}^n - D_{\min}^n} \quad (2)$$

where $U(D_p)$ refers to the percentage of filling volume with particle diameter lower than D_p , D_{\min} is the diameter of the smallest particle in the filling system, and D_{\max} is the maximum particle size. Additionally, the exponent n is considered the distribution modulus of particles, which usually takes 1/2 ~ 1/3. The value of the exponent n will affect the accumulation effect of the particles, so the value n in this work is the optimal 0.37 [30].

The particle size distribution of 5 μm SiO₂, 25 μm BN, and 40 μm Al₂O₃ particles measured by laser particle size analyzer for the three-particle system is shown in Fig. 1b, which are well unimodal distribution. Figure 1c illustrates the SEM images of SiO₂, BN, and Al₂O₃ particles. The size distributions of four particles are consistent with the results tested by the laser granularity analyzer (Fig. 1b, Fig. S1). The filling volume percentages of the three kinds of particles are calculated by Eq. (2), in which D_{\min} is 1.23 μm, and D_{\max} is 93.19 μm. The volume fraction of 1% is usually defined as the lower limit of particle size, so the particle size distribution ranges of 5 μm SiO₂, 25 μm BN, and 40 μm Al₂O₃ are [1.23, 9.17], [9.17, 32.12], [32.12, 93.19], respectively. Combined with the tested densities of an automatic true densitometer, the density of SiO₂, BN, and Al₂O₃ particles is 2.28 g/cm³, 2.29 g/cm³, and 3.94 g/cm³. When the filling content is at 50 wt% in the three-particle system, the weight fraction of SiO₂, BN, and Al₂O₃ are 10.745%, 12.11%, and 27.145%, respectively.

In addition, the two-particle systems compared to the three-particle system consisted of 25 μm BN/5 μm SiO₂, 25 μm BN/5 μm Al₂O₃, and 25 μm BN/40 μm Al₂O₃. The total filling content in all systems was 50 wt%. Table 1 tabulates the specific formulations and designations of different multi-scale EPR composites.

3.2 Morphology characterization of particles and EPR composites

The shape, size, and dispersion of particles greatly influence on the properties of EPR composites, especially the thermal conductivity and electrical insulating properties. Figure 1d shows the SEM images of EPR composites. The brittle fracture interface of EPR is smooth, as shown in Fig. S2a. From the SEM images of EPR composites, it can be seen that the BN are uniformly embedded in the EPR matrix. Since it is difficult to see the cleared spherical particles after brittle fracture of the epoxy composites, spherical particles of SiO₂ or Al₂O₃ were shown by polishing the samples. As Fig. S3 demonstrated, for the polished samples, SiO₂ or Al₂O₃ was uniformly distributed in the EPR matrix. Additionally, the various particle types do not agglomerate within the EPR. This is attributed to the large size of the particles coupled with their small specific surface area, as well as thorough mixing facilitated by the planetary stirrer. Meanwhile, EDS

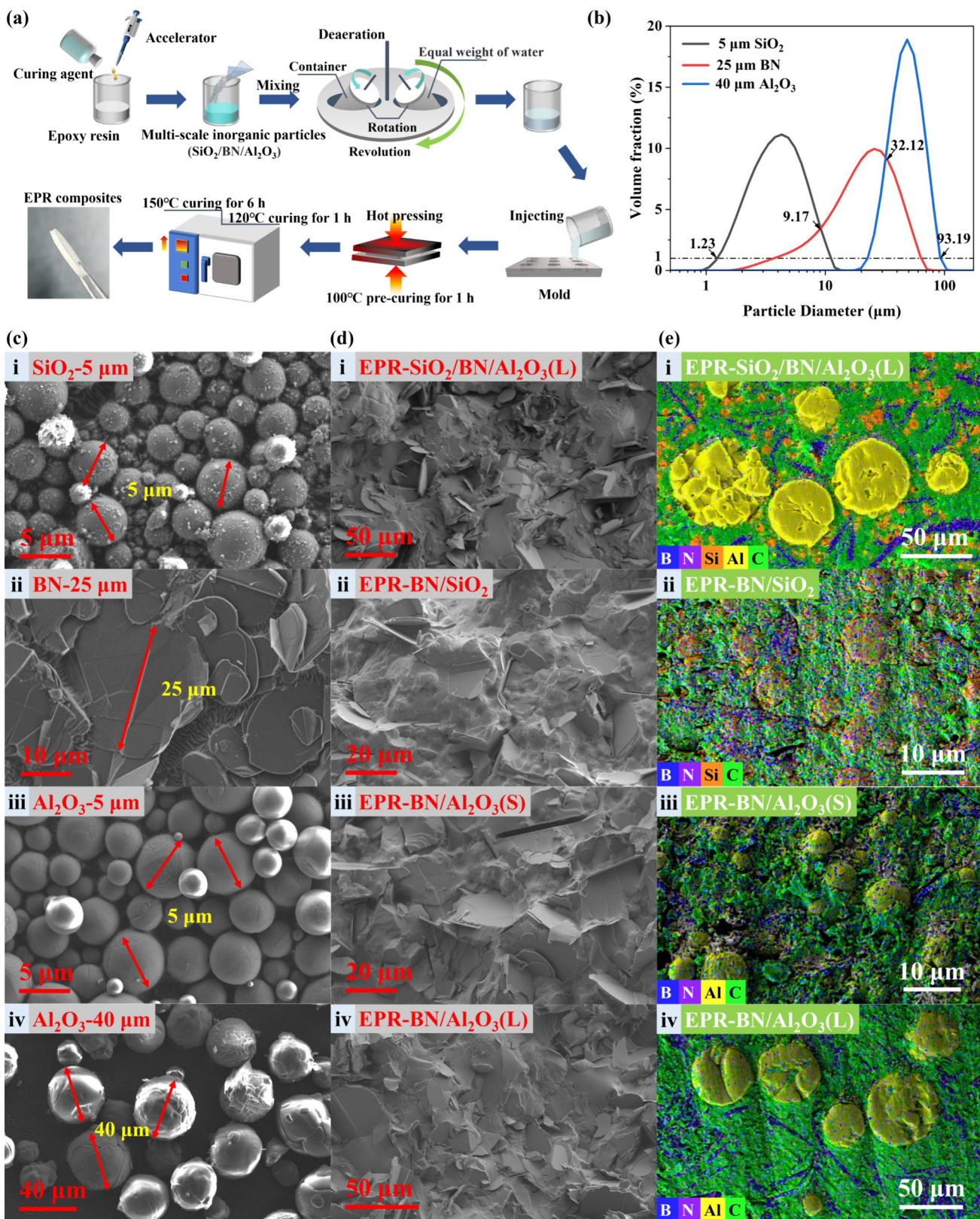


Fig. 1 **a** Preparation process of multi-scale particles EPR composites. **b** Particle size distribution of 5 μm SiO_2 , 25 μm BN, 40 μm Al_2O_3 . **c** SEM images of (i) 5 μm SiO_2 , (ii) 25 μm BN, (iii) 5 μm Al_2O_3 , (iv) 40 μm Al_2O_3 . **d** SEM images of (i) EPR- $\text{SiO}_2/\text{BN}/\text{Al}_2\text{O}_3(L)$, (ii) EPR-BN/ SiO_2 , (iii) EPR-BN/ $\text{Al}_2\text{O}_3(S)$, (iv) EPR-BN/ $\text{Al}_2\text{O}_3(L)$. **e** EDS images of (i) EPR- $\text{SiO}_2/\text{BN}/\text{Al}_2\text{O}_3(L)$, (ii) EPR-BN/ SiO_2 , (iii) EPR-BN/ $\text{Al}_2\text{O}_3(S)$, (iv) EPR-BN/ $\text{Al}_2\text{O}_3(L)$

testing confirmed the elemental distribution of the different particle types within the EPR and its composites, as depicted in Fig. 1e and Fig. S2b. Overall, BN wraps around Al_2O_3 or SiO_2 , forming a network structure within these samples, which is conducive to establishing heat transfer pathways.

3.3 Thermal conductivity and thermal stability

The through-plane thermal conductivity of EPR and its composites was measured by the laser flash method [18, 19]. The thermal conductivity and enhancement rate of multi-scale particles-filled EPR composites at 25°C are shown in Fig. 2a. Due to the disordered arrangement of polymer molecular chains and the weak interaction between molecular chains, the amorphous structure and random vibration of molecular chains reduce the free path of phonons and cause a lot of phonons scattering, resulting in a low thermal conductivity of EPR with only 0.229 W/(m·K) [44]. After adding fillers, the thermal conductivity of the EPR composites significantly improves, mainly benefitted from the construction of a heat transfer network by thermal conductive particles. Specifically, the EPR-BN/ Al_2O_3 (L), comprising 37.5 wt% 40 μm Al_2O_3 and 12.5 wt% 25 μm BN, exhibited the maximal thermal conductivity of 1.177 W/(m·K), which was 413.60% higher than that of pure EPR. Moreover, the thermal conductivity of EPR- SiO_2 /BN/ Al_2O_3 (L), EPR-BN/ SiO_2 , and EPR-BN/ Al_2O_3 (S) was 1.002 W/(m·K), 0.732 W/(m·K), and 1.009 W/(m·K), which were 337.46%, 219.49%, and 340.03% higher than that of pure EPR, respectively. In the two-particle systems, the thermal conductivity of Al_2O_3 is much larger than that of SiO_2 . Additionally, the systems filled with 40 μm Al_2O_3 experience fewer interfaces, resulting in less phonon scattering. Therefore, the thermal conductivity ranking of the EPR composite materials is as follows: EPR-BN/ Al_2O_3 (L)>EPR-BN/ Al_2O_3 (S)>EPR-BN/ SiO_2 . However, compared to the two-particle systems, the three-particle system designed based on the Dinger-Funk model possesses the advantages of a multi-scale composite system. The contact area between the particles increases with the assistance of 40 μm Al_2O_3 and 25 μm BN, which is beneficial for reducing interfacial thermal resistance. At the same time, 5 μm SiO_2 bridges Al_2O_3 and BN to establish efficient heat transfer paths, evidently increasing the thermal conductivity of EPR- SiO_2 /BN/ Al_2O_3 (L) (approaching that EPR-BN/ Al_2O_3 (S)). Figure 2b

depicts a schematic diagram illustrating the internal heat flow and heat transfer network of EPR composites, indicating that multi-scale particles or large-diameter particle filling at 50 wt% are more effective in enhancing the thermal conductivity of composites.

Figure S4 displays the glass transition temperature (T_g) and TGA curve of EPR and its composites. It can be observed from Fig. S4a that the T_g of the two-particle systems is higher than that of pure EPR, whereas the T_g of the three-particle system is only 1.3 °C lower than that of pure EPR. Therefore, filling inorganic particles does not significantly reduce the heat tolerance of pure EPR. It can be considered that the uniform dispersion of fillers restricts the movement of molecular chains during the curing reaction of EPR composites, which improves the crosslinking density and increases the T_g [49]. Moreover, as demonstrated in Fig. S4b, the addition of inorganic fillers into the composites not only enhances the degradation temperature of pure EPR but also improves its thermostability.

3.4 Processing property

The processing performance of EPR composites is crucial for the packaging process of high-frequency power electronic equipment. Therefore, the rheological property (viscosity) of multi-scale particle-filled epoxy composites at different temperatures was tested to evaluate the processability [24, 25]. The viscosities (η) of the uncured EPR composites at 25 °C and 65 °C with shear rate (ω) are shown in Fig. 2c and Fig. S5. The viscosity of pure EPR is found to behave as a Newtonian fluid, remaining unchanged with variations in shear rate. However, after filling 50 wt% of multi-scale particles, the viscosity of the EPR composites is significantly improved. This is due to the reduced spacing between solid particles, which diminishes the fluidity of the epoxy suspension and augments the flow resistance within it. At 25 °C and 10 rad/s, the viscosity of EPR- SiO_2 /BN/ Al_2O_3 (L), EPR-BN/ SiO_2 , EPR-BN/ Al_2O_3 (S), and EPR-BN/ Al_2O_3 (L) is 6409.6 mPa·s, 9124.6 mPa·s, 7457.7 mPa·s, and 7580.9 mPa·s, respectively. It can be concluded that the viscosity of the two-particle systems is higher than that of the three-particle system at 25 °C. Under a given filler loading, the size distribution of filled particles affects the viscosity of the suspension [25, 30, 31]. For example, due to the large length-diameter ratio and

Table 1 Different multi-scale particle-filled compounding systems

Designated code	Weight fraction/%				
	EPR	5 μm SiO_2	25 μm BN	5 μm Al_2O_3	40 μm Al_2O_3
EPR	100	0	0	0	0
EPR- SiO_2 /BN/ Al_2O_3 (L)	50	10.745	12.11	0	27.145
EPR-BN/ SiO_2	50	37.5	12.5	0	0
EPR-BN/ Al_2O_3 (S)	50	0	12.5	37.5	0
EPR-BN/ Al_2O_3 (L)	50	0	12.5	0	37.5

specific surface area, suspensions filled with one-dimensional and two-dimensional fillers exhibit much higher viscosities than suspensions filled with spherical particles under the same particle filling amount [32]. Specially, when the filling content of 25 μm BN is consistent or close, the viscosity of multi-scale particles-filled EPR composites is nearly equivalent. Moreover, the influence of spherical particles on viscosity is much lower than that of two-dimensional materials [28]. Therefore, the viscosity property of the EPR-SiO₂/BN/Al₂O₃(L) composite has been significantly improved with the addition of two types of spherical particles. In addition, considering that the measurement is close to the actual encapsulating situation, the viscosity of EPR composites was measured at the expected encapsulation temperature of 65 °C. With the increase in temperature, the viscosity of EPR composites decreases significantly, and the viscosity of EPR composites at 65 °C is 14 times lower than that at 25 °C.

It can be confidently stated that the design of EPR composites significantly impacts their thermal conductivity and processability. Particularly, achieving higher thermal conductivity while ensuring excellent processing performance poses a challenging problem. For this purpose, Fig. 2d illustrates the viscosity and thermal conductivity of some recently reported EPR and silicone rubber (SR) composites at 25°C and 10 rad/s. It is evident that the multi-scale particle-filled EPR composites prepared in this study achieve higher thermal conductivity at lower viscosity than other materials [25, 28, 31], which suggests that the EPR composites developed hold vast application prospects in power packaging.

3.5 Dielectric breakdown strength/time

There is no doubt that the electrical insulating properties of EPR composites are essential for applications in the power industry. Limited by the output voltage of the high-frequency power supply and the reasonable thickness requirement of the EPR composites, in this study, the electrical insulating properties of the composites were assessed by measuring the breakdown time at high voltage (35 kV/mm), high frequency (10 kHz, 20 kHz), and the breakdown strength at 50 Hz. All the high-voltage tests were carried out at room temperature. The breakdown strength/time was analyzed by a two-parameter Weibull distribution with a 95% confidence interval [36, 42]. The high-frequency electrical insulation test utilized a high-frequency power supply with an output waveform resembling a bipolar square wave, similar to the actual working conditions of SST [7]. The waveform schematic is shown in Fig. S6, and the power supply parameters are provided in Table S1. As illustrated in Fig. 2e, the breakdown strength of EPR, EPR-SiO₂/BN/Al₂O₃(L), EPR-BN/SiO₂, EPR-BN/Al₂O₃(S), and EPR-BN/Al₂O₃(L) at 50 Hz are 84.66 kV/mm, 80.66 kV/mm, 87.54 kV/mm, 82.61 kV/mm, and 78.77 kV/mm, respectively. With the particles filling of 50 wt%, the breakdown strength of

EPR-BN/SiO₂ increased by 3.4% compared with pure EPR, and the other composites decreased. The breakdown strength of EPR-BN/Al₂O₃(L) is the lowest, at only 6.96% lower than that of pure EPR, which substantiates that the composites prepared by filling with multi-scale particles still maintain excellent electrical insulating properties at 50 Hz. Moreover, Fig. S7 demonstrates the breakdown time of EPR, EPR-SiO₂/BN/Al₂O₃(L), EPR-BN/SiO₂, EPR-BN/Al₂O₃(S), EPR-BN/Al₂O₃(L) at 10kHz, 35kV/mm is 18.61 s, 23.34 s, 43.13 s, 22.28 s, 15.56 s, relative to pure EPR improved by 25.42%, 131.76%, 19.72%, and –16.39%, respectively. As the frequency increases, Fig. 2f shows that the breakdown time of pure EPR and its composites at 20 kHz is 15.99 s, 21.46 s, 42.21 s, 23.88 s, and 12.16 s, which is improved by 34.21%, 163.97%, 49.34%, and –23.95% concerning pure EPR, respectively.

Obviously, the electrical insulating properties of EPR under bipolar high-frequency, high-voltage square waves have been improved effectively by the filling of multi-scale particles. In particular, the EPR-BN/SiO₂ has the longest breakdown time either at 10 kHz or 20 kHz, and its electrical insulating properties are optimal even when analyzed in combination with the breakdown strength at 50 Hz. Meanwhile, the breakdown time at high frequencies and the breakdown strength at 50 Hz verified that the electrical insulating properties of the EPR-SiO₂/BN/Al₂O₃(L) with a three-particle system and the EPR-BN/Al₂O₃(S) with a two-particle system are close.

3.6 Integrated performance

The simple method of multi-scale particle filling is used to significantly enhance the thermal conductivity and electrical insulating properties of EPR under high frequency and high voltage with excellent processing performance and cost-effectiveness, as depicted in Fig. 3 for specific comparison. In addition, the method also has little effect on the heat tolerance of the EPR composites. The EPR-BN/Al₂O₃(L) achieves the highest thermal conductivity of 1.177 W/(m·K) but has the worst electrical insulating properties. The thermal conductivity and electrical insulating properties of the three-particle system EPR-SiO₂/BN/Al₂O₃(L) are similar to the two-particle system EPR-BN/Al₂O₃(S). However, although the thermal conductivity of EPR-BN/SiO₂ is only 0.732 W/(m·K), the electrical insulating performance is best at a high voltage of 10 to 20 kHz.

4 Discussion

4.1 Effect of temperature rise on high-frequency electrical insulating performance

As the temperature increases significantly in SST during the work process, high temperatures are harmful to the electrical

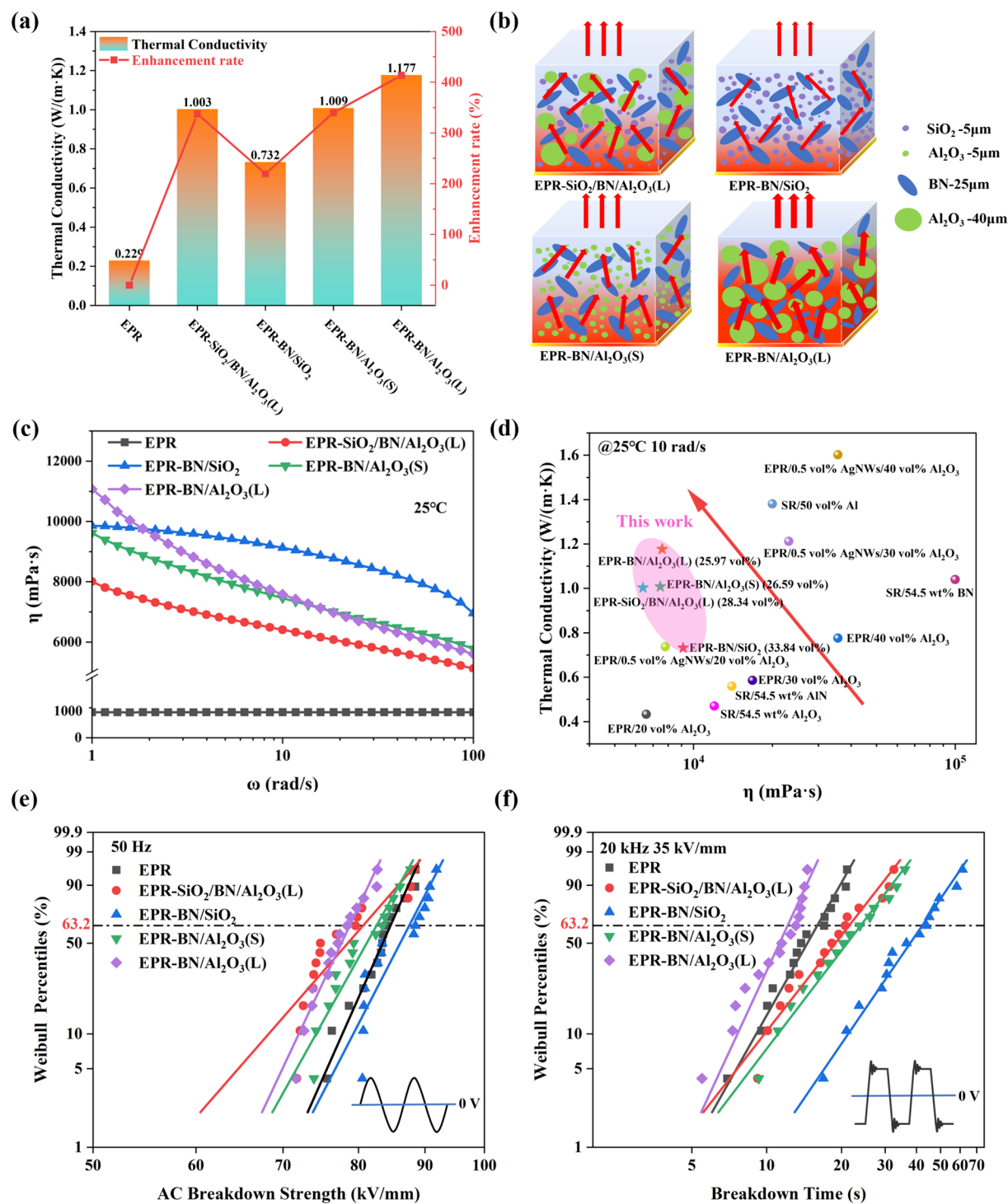


Fig. 2 **a** Thermal conductivity and enhancement rate of EPR composites. **b** Schematic diagram about the internal heat flow and heat transfer network of epoxy composites. **c** Viscosity of EPR composites at 25 °C. **d** Comparison among thermal conductivity and viscosity of EPR composites with existing literatures [25, 28, 31]. **e** Breakdown strength of EPR composites at 50 Hz. **f** Breakdown time of EPR composites at 20 kHz and 35 kV/mm

insulating properties of the material. The dielectrics generate dielectric loss per unit of time and volume at high frequencies, as shown in Eq. (3) [43].

$$P_{dl} = \frac{\omega C U^2}{V} = \frac{\omega \frac{\epsilon_0 \epsilon'' S}{d} E^2 d^2}{S d} = \omega \epsilon_0 \epsilon'' E^2 \quad (3)$$

where P_{dl} is the electrical polarization loss generated by the dielectrics in unit time and unit volume, ω is the angular frequency ($\omega = 2\pi f$), ϵ_0 is the vacuum dielectric constant, ϵ'' is the imaginary part of the dielectric constant ($\epsilon^* = \epsilon' - j\epsilon''$) of the composite, indicating the loss, and E is the electric strength applied to it. From Eq. (3), it is found that the higher ϵ'' can lead to an increase in the P_{dl} , which causes the severe heating of the power equipment during high-frequency operation.

Figure S8a shows the dielectric properties of the EPR composites at room temperature in the frequency range 10⁰ to 10⁶ Hz. The dielectric constant (ϵ') of EPR composites decreases with increasing frequency. Except for EPR-BN/SiO₂, the ϵ' of other samples is higher than pure EPR. Herein, based on the frequency band of SST, we focus on the variation of ϵ'' at 10 kHz and 20 kHz from 20 to 200 °C, as shown in Fig. S8b and Fig. 4a. At 10 kHz and 20 kHz, the trend of ϵ'' of EPR composites with increasing temperature is close to each other. The ϵ'' of EPR composites at 20 kHz is slightly lower than that at 10 kHz. Typically, the ϵ'' at high frequencies is related to the β relaxation due to the movement of epoxy side chain segments [42, 50]. Therefore, the decrease in ϵ'' of the composites at high frequencies may be due to the filled particles limiting the local movement of the side chains on epoxy. The lowest ϵ'' for the EPR-BN/SiO₂ composites can be explained by the fact that SiO₂ has a lower scale size and density than Al₂O₃, so that for the same weight fraction, the more significant number of particles in the filled SiO₂ has the most pronounced restriction on the polymer chain movement. However, the α relaxation of the EPR is more pronounced at temperatures higher than T_g , leading to a significant increase in the ϵ'' of the composites [50].

When a high-frequency, high-voltage, and bipolar square wave is applied to EPR composites, the heat production of the dielectric loss competes with the heat dissipation of the thermal conductivity to determine the temperature rise of the material. An infrared camera was used to record the surface temperature of different samples over time to detect the temperature rise of multi-scale particles-filled EPR composites under high frequency and high voltage. Meanwhile, the heating test was carried out at 10 kV/mm to avoid surface flashover.

Figure S8c and Fig. 4b show the variation of surface temperature of EPR composites with time at 10 kHz and 20 kHz, respectively. As shown in Fig. 4c, the EPR rises to 66.7 °C at 20 kHz, the EPR-BN/SiO₂ with the lowest dielectric loss rises to 56.2 °C, and the EPR-BN/Al₂O₃(L) with the highest thermal conductivity reaches 56 °C. According to the in-set picture in Fig. 4a, the dielectric loss of EPR-BN/SiO₂ is the lowest near 60 °C, followed by EPR-SiO₂/BN/Al₂O₃(L), while EPR-BN/Al₂O₃(S), EPR-BN/Al₂O₃(L), and EPR are higher and close to each

other. As demonstrated in Fig. S8d, the EPR rises to 48.5 °C at 10 kHz, and the temperature rises of EPR-SiO₂/BN/Al₂O₃(L), EPR-BN/SiO₂, EPR-BN/Al₂O₃(S), and EPR-BN/Al₂O₃(L) are 40.1 °C, 40.7 °C, 40.4 °C, and 40.5 °C, respectively. The temperature of the EPR composites did not reach T_g in the temperature rise test at 10 kV/mm. Meanwhile, the temperature rises of all the EPR composites are close to each other at 10 kHz and 20 kHz, respectively. The EPR-BN/SiO₂ composite has the lowest dielectric loss, resulting in low heat generation and compensating for the disadvantage of lower thermal conductivity. Both at 10 kHz and 20 kHz, the steady-state temperatures of the EPR-BN/SiO₂ composite are less than 1 °C different from that of EPR-SiO₂/BN/Al₂O₃(L), EPR-BN/Al₂O₃(S), and EPR-BN/Al₂O₃(L) composites. However, the electrical insulation failure of EPR and its composites is significantly accelerated at 35 kV/mm, possibly related to the higher temperature than T_g . As the temperature is higher than T_g , the dielectric loss of the EPR composites rises significantly, leading to more severe heating and will even cause EPR decomposition. Therefore, reducing the dielectric loss and increasing the thermal conductivity suppress the heating of the material at high frequencies, which in turn improves its breakdown time.

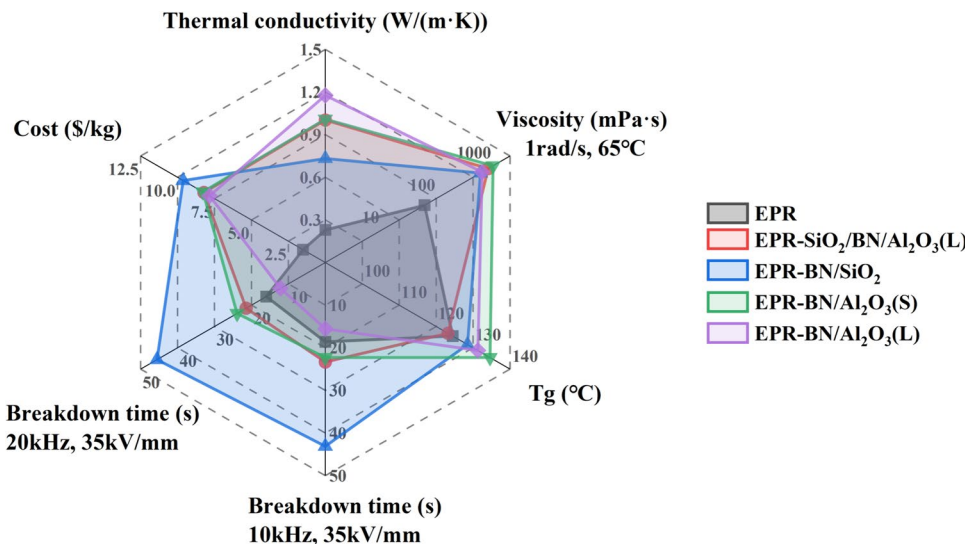
To make the above conclusions more rigorous, this study considers that the actual composite is not an ideal dielectric and, therefore, adds the conductive loss at high voltages, which can be easily obtained from Ohm's law, as shown in Eq. (4) [51].

$$P_c = \frac{I^2 R}{V} = \frac{\frac{d}{Sd}}{\frac{d}{Sd}} = \gamma E^2 \quad (4)$$

where P represents the Joule heat generated by the dielectric in unit time and volume, γ represents the conductivity, and E represents the electric strength. Equation (4) is similar to Eq. (3) in that it is related to E as a square. Comparison of γ and the magnitude of $\omega\epsilon_0\epsilon''$ at different frequencies can determine the percentage of loss at high frequencies.

The DC conductivity of the composites at 10 kV/mm is demonstrated in Fig. 4d. The DC conductivity of EPR and its composites was enhanced from 10⁻¹⁵–10⁻¹⁶ S/m to 10⁻⁹–10⁻¹⁰ S/m from 25 to 200 °C. Below 100 °C, the DC conductivity of EPR composites is slightly higher than that of pure EPR. When the temperature exceeded 120 °C (T_g), the conductivity of EPR composites appeared to be lower than that of pure EPR. In particular, the DC conductivity of EPR-BN/SiO₂ and EPR-BN/Al₂O₃(S) was lower than that of other composites due to the filling of small size (5 μm) particles. Figure 4e illustrates the variation of the ratio of γ to $\omega\epsilon_0\epsilon''$ with temperature rise for different samples at 20 kHz. Until 200 °C, the order of magnitude of $\gamma/\omega\epsilon_0\epsilon''$ is in the range of 10⁻²–10⁻³, which

Fig. 3 Radar plot for the comparison the integrated performance for EPR composites



means that the percentage of conductive losses in the high-frequency and high-voltage scenarios of this study is meager and negligible. Meanwhile, the relationship between $\gamma/\omega\epsilon_0\epsilon''$ and the temperature of EPR composites at 10 kHz is consistent with Fig. 4e, as shown in Fig. S9. Therefore, the data analysis was used to re-verify that the design of high-frequency electrical insulating materials should focus on the magnitude of the dielectric loss of the materials.

In addition, the temperature rise of the composites was also calculated by finite element simulation, as shown in Fig. S10, which verified that the heating trend of the EPR composites was consistent with the actual test and the temperature difference between the composite systems was low. Furthermore, the simulated temperature rise of EPR is close to the actual test results. However, the steady-state temperature of the EPR composites is much lower than the actual test results, which may be related to the inhomogeneous electric field inside the composites, as described next.

4.2 Effect of electric field distribution on high-frequency electrical insulating performance

From the previous results, the electrical insulation performance at 10 kHz and 20 kHz is best for EPR-BN/SiO₂, followed by EPR-BN/Al₂O₃(S) and EPR-SiO₂/BN/Al₂O₃(L), then EPR and the worst is EPR-BN/Al₂O₃(L). However, the ϵ'' of EPR-BN/Al₂O₃(L) is close to EPR at low temperatures and lower than EPR at temperatures above T_g . Meanwhile, the thermal conductivity of EPR-BN/Al₂O₃(L) is much higher than EPR. Therefore, in addition to dielectric loss and thermal conductivity of material, other factors should affect the electrical insulating properties at high frequency

and high voltage. To further understand the rapid damage of electrical insulation materials under high frequency and high voltage, this work analyzed the electric field distribution of EPR composites through finite element simulation. The theoretical basis for the electric field distribution in composites at high frequency and high voltage is shown in the supporting information (Fig. S11), and the basic idea is to analyze and simplify the interfacial conditions of different dielectrics under the electrically quasi-static field. The conclusion illustrates that the electric field distribution at the interface of different dielectrics is inversely proportional to the relative permittivity. In this study, a simplified model is used to calculate the electric field distribution, and the thickness of the EPR composites is 100 μm and the voltage is 3.5 kV. The relative dielectric constants of SiO₂, BN, and Al₂O₃ were taken as 3.9, 4.8, and 9.8, respectively [52–54]. As demonstrated in Fig. 5a, the electric field distribution of EPR-BN/SiO₂ is the most uniform, followed by EPR-BN/Al₂O₃(S) with EPR-SiO₂/BN/Al₂O₃(L), and the worst is still EPR-BN/Al₂O₃(L), which is consistent with the test results at high frequency and high voltage. Since the relative dielectric constants of SiO₂ and EPR (3.87) are closest, the low electric field at the interface between SiO₂ particles and epoxy matrix is favorable for prolonging the breakdown time at high frequency and high voltage. A comparison of EPR-BN/Al₂O₃(S) and EPR-BN/Al₂O₃(L) compounded with different Al₂O₃ sizes shows that filling particles with small sizes results in lower electric field distortion. In EPR-SiO₂/BN/Al₂O₃(L), the negative effect of large-scale Al₂O₃ on the electrical insulating properties is partially canceled out by the addition of SiO₂, which reduces the distortion of the electric field.

Considering the complexity of high-frequency breakdown time testing, this study further analyzes the breakdown development in conjunction with Schottky's thermal

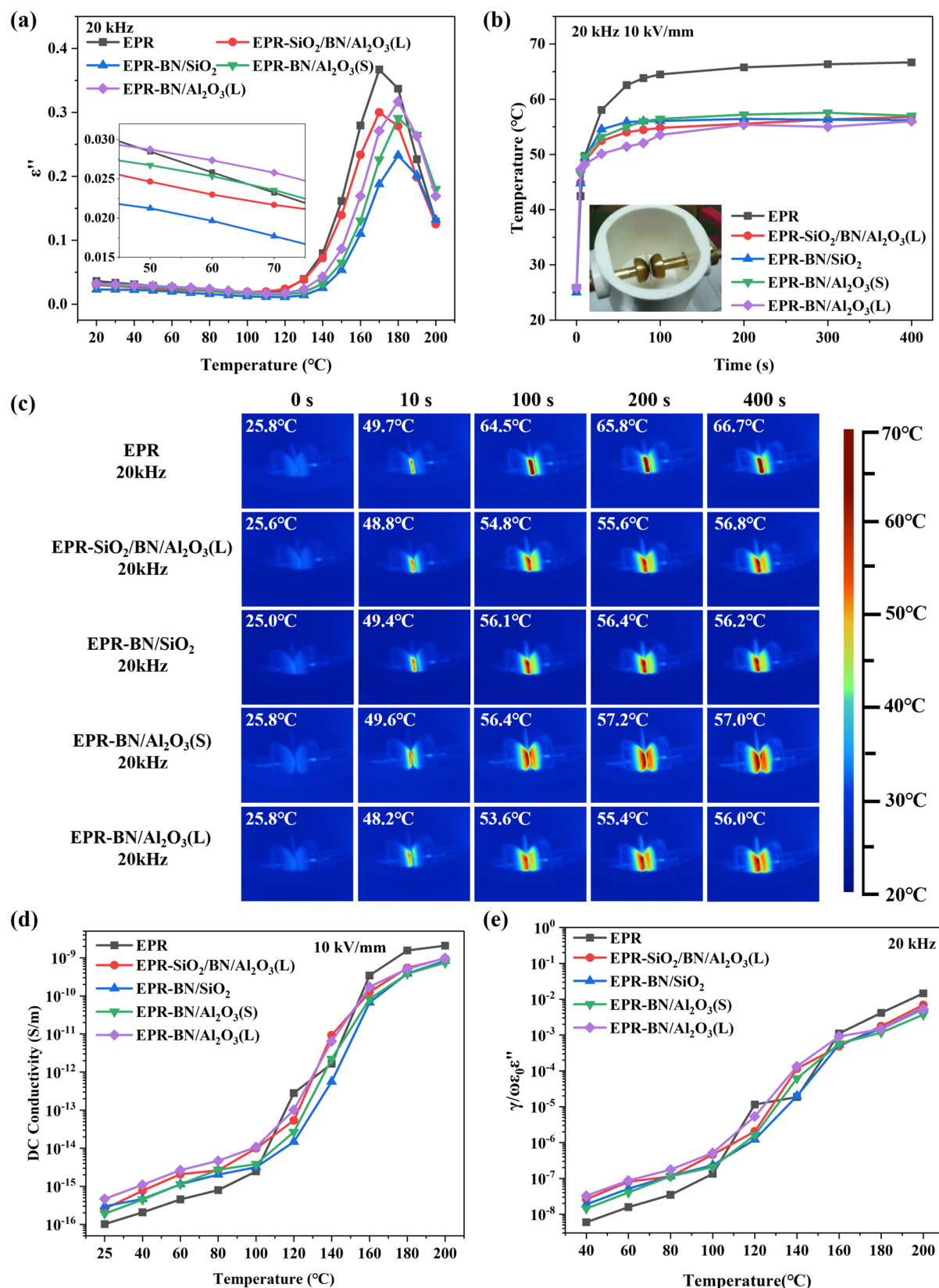


Fig. 4 **a** The ϵ'' of EPR composites varies with temperature at 20 kHz. **b** Variation of surface temperature of EPR composites with time at 20 kHz. **c** Infrared thermal image of EPR composites at 20 kHz, 10

kV/mm. **d** Temperature-dependent DC conductivity of EPR composites at 10 kV/mm. **e** The ratio of γ to $\omega\epsilon_0\epsilon''$ for EPR composites varies with increasing temperature at 20 kHz

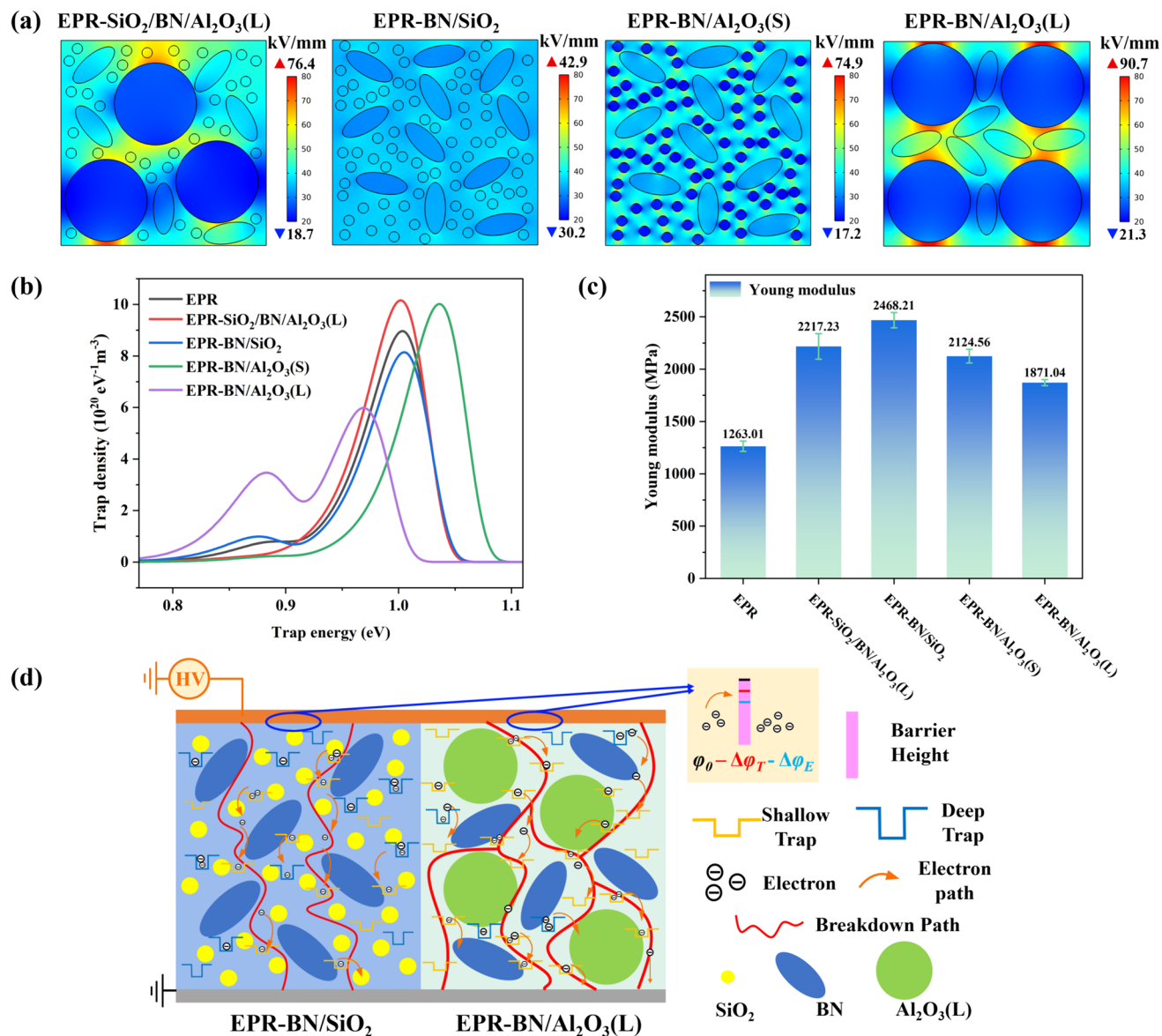


Fig. 5 **a** Electric field distribution, **b** trap parameters, **c** Young's modulus of EPR composites. **d** The schematics of carrier injection and transport in EPR-BN/Al₂O₃(L) and EPR-BN/SiO₂ under high frequency and high voltage

emission theory. In this theory, the injection of charge in the polymer is related to the interfacial barrier height, temperature, applied electric field strength, etc., as shown in Eq. (5) [41].

$$J = AT^2 \exp\left(\frac{-\varphi_0 + q\sqrt{qE/4\pi\epsilon'\epsilon_0}}{k_B T}\right) \quad (5)$$

where J is the current density, A is Richardson's constant, T is the absolute temperature, q is the electron charge, φ_0 is the interfacial barrier height, E is the interfacial electric field between the electrodes and the material, k_B is the

Boltzmann's constant, ϵ_0 is the vacuum dielectric constant, and ϵ' is the relative dielectric constant.

At high frequencies, the interfacial barrier between the electrode and the composite material is reduced from φ_0 to $\varphi_0 - \Delta\varphi_T - \Delta\varphi_E$ due to the temperature rise and the high voltage stress [41, 55]. Reducing the interfacial barrier height will significantly increase the hopping injection of carriers through the electrodes, and the electrothermal emission will also generate more carriers. In particular, shallow and deep traps in the EPR composites capture the injected carriers [56–58]. As shown in Fig. 5b, the trap energy is 0.8–0.9 eV for shallow traps and 0.9–1.1 eV for deep traps. There

are more shallow traps in EPR-BN/Al₂O₃(L) and more deep traps in EPR-BN/SiO₂. Due to the high electric field distortion of EPR-BN/Al₂O₃(L) and the large number of shallow traps increasing the carrier mobility, the electrical insulation failure of the sample is accelerated. The EPR-BN/SiO₂ with more deep traps has low carrier mobility and low electric field distortion, which prolongs the electrical insulation life under high frequency.

At the same time, the magnitude of Young's modulus will also affect the development of the breakdown paths, as shown in Fig. 5c [59, 60]. The EPR-BN/SiO₂ has a larger Young's modulus than EPR-BN/Al₂O₃(L), which means the filling of small micron-scale particles helps to extend the breakdown paths and then increases the breakdown time under high frequency and high voltage. According to the above analysis of the high-frequency breakdown process, the schematic diagram of carrier injection and transport is summarized in Fig. 5d. Therefore, small micron-scale particles with dielectric constants close to EPR should be preferred when designing high-voltage electrical insulation materials from 10 to 20 kHz.

5 Conclusion

In summary, the EPR composites were prepared by a simple multi-scale particles-filled method, which improves the thermal conductivity and electrical insulating properties of EPR under high frequency and high voltage with good processing performance. A small amount of two-dimensional filler (BN) and spherical fillers (SiO₂, Al₂O₃) were used to build a thermal conductive network to increase the contact area between thermal conductive particles, making the thermal conductivity up to 1.177 W/(m·K), which is 5 times that of EPR. It has been verified that adding a small amount of two-dimensional materials can simultaneously enhance heat transfer efficiency and ensure good processability. Focusing on the practical application of solid-state transformer (SST), the main factors influencing the electrical insulation performance under bipolar square waves with frequencies of 10 kHz and 20 kHz were discussed. The design of insulating materials at high frequencies should not only aim for high thermal conductivity but also focus on the magnitude of dielectric loss. The addition of particles with a dielectric constant similar to that of the polymer matrix (SiO₂), along with small size particles (5 μm), facilitates the reduction of electric field distortions and significantly enhances the electrical insulation properties at high frequencies and high voltages (the composite maximum improvement of 163.97% relative to EPR). The small-sized SiO₂ (5 μm) and large-sized BN (25 μm) are the ideal combination of fillers. This

study provides a practical material for SST and a theoretical basis for designing high-frequency electrical insulating materials.

Supplementary Information The online version contains supplementary material available at <https://doi.org/10.1007/s42114-024-00914-6>.

Acknowledgements The researchers would like to acknowledge the Experimental Analysis Platform of Tsinghua University for providing micro-morphological and thermodynamic analyses and the Department of Electrical Engineering for providing the ISPD trap test.

Authors contributions Yan-Hui Song conceived and prepared the materials, completed experimental testing and data analysis, and wrote the manuscript. Li-Juan Yin, Shao-Long Zhong, and Qi-Kun Feng contributed to the revision of the manuscript and analyzed the data. Haidong Wang, Pingjia Zhang, and Hai-Ping Xu reviewed and revised the manuscript. Tong Liang assisted in experimental testing. Zhi-Min Dang proposed manuscript revisions and provided and supervised the project. All authors have reviewed the manuscript.

Funding This work was supported by the Zhongguancun National Independent Innovation Demonstration Zone open laboratory concept verification project, the State Key Lab of Power System Operation and Control, Tsinghua University (No. SKLD21M01), and China Postdoctoral Science Foundation (No. 2022TQ0167 and No. 2022M721777).

Data availability No datasets were generated or analysed during the current study.

Declarations

Competing interests The authors declare no competing interests.

Open Access This article is licensed under a Creative Commons Attribution 4.0 International License, which permits use, sharing, adaptation, distribution and reproduction in any medium or format, as long as you give appropriate credit to the original author(s) and the source, provide a link to the Creative Commons licence, and indicate if changes were made. The images or other third party material in this article are included in the article's Creative Commons licence, unless indicated otherwise in a credit line to the material. If material is not included in the article's Creative Commons licence and your intended use is not permitted by statutory regulation or exceeds the permitted use, you will need to obtain permission directly from the copyright holder. To view a copy of this licence, visit <http://creativecommons.org/licenses/by/4.0/>.

References

1. Falcones S, Ayyanar R, Mao X (2013) A DC–DC multiport-converter-based solid-state transformer integrating distributed generation and storage. IEEE Trans Power Electron 28(5):2192–2203. <https://doi.org/10.1109/tpel.2012.2215965>
2. Li Z, Hsieh E, Li Q, Lee FC (2023) High-frequency transformer design with medium-voltage insulation for resonant converter in solid-state transformer. IEEE Trans Power Electron 38(8):9917–9932. <https://doi.org/10.1109/TPEL.2023.3279030>
3. Zheng L, Marellapudi A, Chowdhury VR, Bilakanti N, Kandula RP, Saeedifard M, Grijalva S, Divan D (2022) Solid-state transformer and hybrid transformer with integrated energy storage in

- active distribution grids: technical and economic comparison, dispatch, and control. *IEEE J Emerg Sel Top Power Electron* 10(4):3771–3787. <https://doi.org/10.1109/JESTPE.2022.3144361>
- 4. Feng J, Chu WQ, Zhang Z, Zhu ZQ (2017) Power electronic transformer-based railway traction systems: challenges and opportunities. *IEEE J Emerg Sel Top Power Electron* 5(3):1237–1253. <https://doi.org/10.1109/jestpe.2017.2685464>
 - 5. Liserre M, Buticchi G, Andresen M, Carne GD, Costa LF, Zou ZX (2016) The smart transformer: impact on the electric grid and technology challenges. *IEEE Ind Electron Mag* 10(2):46–58. <https://doi.org/10.1109/MIE.2016.2551418>
 - 6. Leibl M, Ortiz G, Kolar JW (2017) Design and experimental analysis of a medium-frequency transformer for solid-state transformer applications. *IEEE J Emerg Sel Top Power Electron* 5(1):110–123. <https://doi.org/10.1109/jestpe.2016.2623679>
 - 7. Zhao Y, Zhang G, Guo R, Yang F (2019) The breakdown characteristics of thermostable insulation materials under high-frequency square waveform. *IEEE Trans Dielectr Electr Insul* 26(4):1073–1080. <https://doi.org/10.1109/tdei.2019.007856>
 - 8. Guo Z, Yu R, Xu W, Feng X, Huang AQ (2021) Design and optimization of a 200-kw medium-frequency transformer for medium-voltage SiC PV inverters. *IEEE Trans Power Electron* 36(9):10548–10560. <https://doi.org/10.1109/tpe.2021.3059879>
 - 9. Guillod T, Faerber R, Rothmund D, Krismer F, Franck CM, Kolar JW (2020) Dielectric losses in dry-type insulation of medium-voltage power electronic converters. *IEEE J Emerg Sel Top Power Electron* 8(3):2716–2732. <https://doi.org/10.1109/jestpe.2019.2914997>
 - 10. Awais M, Chen X, Dai C, Wang Q, Meng F-B, Hong Z, Paramane A, Tanaka Y (2022) Investigating optimal region for thermal and electrical properties of epoxy nanocomposites under high frequencies and temperatures. *Nanotechnology*. 33(13):135705. <https://doi.org/10.1088/1361-6528/ac45c3>
 - 11. Teng C, Zhou Y, Li S, Zhang L, Zhang Y, Zhou Z, Zhao L (2020) Regulation of temperature resistivity characteristics of insulating epoxy composite by incorporating positive temperature coefficient material. *IEEE Trans Dielectr Electr Insul* 27(2):512–520. <https://doi.org/10.1109/tdei.2020.008600>
 - 12. Li T, Li P, Sun R, Yu S (2023) Polymer-based nanocomposites in semiconductor packaging. *IET Nanodielectrics* 6(3):147–158. <https://doi.org/10.1049/nde2.12050>
 - 13. Tanaka S, Hojo F, Takezawa Y, Kanie K, Muramatsu A (2018) Highly oriented liquid crystalline epoxy film: robust high thermal-conductive ability. *ACS Omega* 3(3):3562–3570. <https://doi.org/10.1021/acsomega.7b02088>
 - 14. Islam AM, Lim H, You N-H, Ahn S, Goh M, Hahn JR, Yeo H, Jang SG (2018) Enhanced thermal conductivity of liquid crystalline epoxy resin using controlled linear polymerization. *ACS Macro Lett* 7(10):1180–1185. [https://doi.org/10.1021/acsmacrollett.8b00456](https://doi.org/10.1021/acsmacrolett.8b00456)
 - 15. Hou J, Li G, Yang N, Qin L, Grami ME, Zhang Q, Wang N, Qu X (2014) Preparation and characterization of surface modified boron nitride epoxy composites with enhanced thermal conductivity. *RSC Adv* 4(83):44282–44290. <https://doi.org/10.1039/c4ra07394k>
 - 16. Bian W, Yao T, Chen M, Zhang C, Shao T, Yang Y (2018) The synergistic effects of the micro-BN and nano-Al₂O₃ in micro-nano composites on enhancing the thermal conductivity for insulating epoxy resin. *Comp Sci Technol.* 168:420–428. <https://doi.org/10.1016/j.compscitech.2018.10.002>
 - 17. Huang X, Zhi C, Jiang P, Golberg D, Bando Y, Tanaka T (2012) Polyhedral oligosilsesquioxane-modified boron nitride nanotube based epoxy nanocomposites: an ideal dielectric material with high thermal conductivity. *Adv Func Mater* 23(14):1824–1831. <https://doi.org/10.1002/adfm.201201824>
 - 18. Han J, Du G, Gao W, Bai H (2019) An anisotropically high thermal conductive boron nitride/epoxy composite based on nacre-mimetic 3D network. *Advanced Functional Materials* 29(13). <https://doi.org/10.1002/adfm.201900412>
 - 19. Xu X, Hu R, Chen M, Dong J, Xiao B, Wang Q, Wang H (2020) 3d boron nitride foam filled epoxy composites with significantly enhanced thermal conductivity by a facile and scalable approach. *Chem Eng J* 397. <https://doi.org/10.1016/j.cej.2020.125447>
 - 20. Wang H, Li L, Wei X, Hou X, Li M, Wu X, Li Y, Lin C-T, Jiang N, Yu J (2020) Combining alumina particles with three-dimensional alumina foam for high thermally conductive epoxy composites. *ACS Appl Polym Mater* 3(1):216–225. <https://doi.org/10.1021/acsapm.0c01055>
 - 21. Lule Z, Kim J (2019) Thermally conductive and highly rigid poly-lactic acid (PLA) hybrid composite filled with surface treated alumina/nano-sized aluminum nitride. *Composites Part A: Applied Science and Manufacturing* 124. <https://doi.org/10.1016/j.compositesa.2019.105506>
 - 22. Hong J-P, Yoon S-W, Hwang T, Oh J-S, Hong S-C, Lee Y, Nam J-D (2012) High thermal conductivity epoxy composites with bimodal distribution of aluminum nitride and boron nitride fillers. *Thermochimica Acta* 537:70–75. <https://doi.org/10.1016/j.tca.2012.03.002>
 - 23. Luan BCD, Huang J, Zhang J (2015) Enhanced thermal conductivity and wear resistance of polytetrafluoroethylene composites through boron nitride and zinc oxide hybrid fillers. *Journal of Applied Polymer Science*. 132(30):app.42302. <https://doi.org/10.1002/app.42302>
 - 24. Guo Q, Zhu P, Li G, Huang L, Zhang Y, Lu DD, Sun R, Wong C (2015) One-pot synthesis of bimodal silica nanospheres and their effects on the rheological and thermal–mechanical properties of silica–epoxy composites. *RSC Adv* 5(62):50073–50081. <https://doi.org/10.1039/c5ra06914a>
 - 25. Hu Y, Chen C, Wen Y, Xue Z, Zhou X, Shi D, Hu G-H, Xie X (2021) Novel micro-nano epoxy composites for electronic packaging application: balance of thermal conductivity and processability. *Composites Science and Technology* 209. <https://doi.org/10.1016/j.compscitech.2021.108760>
 - 26. Wong CP, Bollampally RS (1999) Comparative study of thermally conductive fillers for use in liquid encapsulants for electronic packaging. *IEEE TRANSACTIONS ON ADVANCED PACKAGING*. 22(1):54. <https://doi.org/10.1109/6040.746543>
 - 27. Lin Z, McNamara A, Liu Y, Moon K-S, Wong C-P (2014) Exfoliated hexagonal boron nitride-based polymer nanocomposite with enhanced thermal conductivity for electronic encapsulation. *Composites Science and Technology* 90:123–128. <https://doi.org/10.1016/j.compscitech.2013.10.018>
 - 28. Li Y-T, Liu W-J, Shen F-X, Zhang G-D, Gong L-X, Zhao L, Song P, Gao J-F, Tang L-C (2022) Processing, thermal conductivity and flame retardant properties of silicone rubber filled with different geometries of thermally conductive fillers: a comparative study. *Composites Part B: Engineering* 238. <https://doi.org/10.1016/j.compositesb.2022.109907>
 - 29. Y. Wen, C. Chen, Y. Feng, Z. Xue, X. Zhou, X. Xie, Y.-W. Mai. (2020) Effects of selective distribution of alumina micro-particles on rheological, mechanical and thermal conductive properties of asphalt/SBS/alumina composites. *Composites Science and Technology*. 186. <https://doi.org/10.1016/j.compscitech.2019.107917>
 - 30. Feng Q-K, Liu C, Zhang D-L, Song Y-H, Sun K, Xu H-P, Dang Z-M (2022) Particle packing theory guided multiscale alumina filled epoxy resin with excellent thermal and dielectric performances. *J Materiomics* 8(5):1058–1066. <https://doi.org/10.1016/j.jmat.2022.02.008>
 - 31. Mao L, Han J, Zhao D, Song N, Shi L, Wang J (2018) Particle packing theory guided thermal conductive polymer preparation and related properties. *ACS Appl Mater Interfaces* 10(39):33556–33563. <https://doi.org/10.1021/acsami.8b10983>

32. Wen Y, Chen C, Ye Y, Xue Z, Liu H, Zhou X, Zhang Y, Li D, Xie X, Mai YW (2022) Advances on thermally conductive epoxy-based composites as electronic packaging underfill materials-a review. *Adv Mater* 34(52):e2201023. <https://doi.org/10.1002/adma.202201023>
33. Thabet A, Salem N (2020) Experimental progress in electrical properties and dielectric strength of polyvinyl chloride thin films under thermal conditions. *Trans Electr Electron Mater* 21(2):165–174. <https://doi.org/10.1007/s42341-019-00163-1>
34. Thabet A, Salem N (2020) Experimental verification on dielectric breakdown strength using individual and multiple nanoparticles in polyvinyl chloride. *Trans Electr Electron Mater* 21(3):274–282. <https://doi.org/10.1007/s42341-020-00176-1>
35. Fang L, Wu C, Qian R, Xie L, Yang K, Jiang P (2014) Nano-micro structure of functionalized boron nitride and aluminum oxide for epoxy composites with enhanced thermal conductivity and breakdown strength. *RSC Adv* 4(40):21010–21017. <https://doi.org/10.1039/c4ra01194e>
36. T. Yao, K. Chen, T. Niu, Y. Yang. (2021) Effects of frequency and thermal conductivity on dielectric breakdown characteristics of epoxy/cellulose/BN composites fabricated by ice-templated method. *Composites Science and Technology*. 213. <https://doi.org/10.1016/j.compscitech.2021.108945>
37. M. Awais, X. Chen, Z. Hong, Q. Wang, Y. Shi, F.-B. Meng, C. Dai, A. Paramane (2022) Synergistic effects of micro-hBN and core-shell nano-TiO₂@SiO₂ on thermal and electrical properties of epoxy at high frequencies and temperatures. *Composites Science and Technology*. 227. <https://doi.org/10.1016/j.compscitech.2022.109576>
38. Nazir MT, Khalid A, Akram S, Mishra P, Kabir II, Yeoh GH, Phung BT, Wong KL (2023) Electrical tracking, erosion and flammability resistance of high voltage outdoor composite insulation: research, innovation and future outlook. *Mater Sci Eng R: Rep* 156:100757. <https://doi.org/10.1016/j.mser.2023.100757>
39. Wang Z, Yang M, Cheng Y, Liu J, Xiao B, Chen S, Huang J, Xie Q, Wu G, Wu H (2019) Dielectric properties and thermal conductivity of epoxy composites using quantum-sized silver decorated core/shell structured alumina/polydopamine. *Composites Part A: Applied Science and Manufacturing* 118:302–311. <https://doi.org/10.1016/j.compositesa.2018.12.022>
40. Wang Z, Iizuka T, Kozako M, Ohki Y, Tanaka T (2011) Development of epoxy/BN composites with high thermal conductivity and sufficient dielectric breakdown strength part I -sample preparations and thermal conductivity. *IEEE Transactions on Dielectrics and Electrical Insulation*. 18(6):1963. <https://doi.org/10.1109/TDEI.2011.6118634>
41. M. Awais, X. Chen, Y. Shi, Q. Wang, G. Zhu, F. B. Meng, Z. Hong, A. Paramane (2022) Influence of dielectric barrier effect and thermally-conductive network on thermal and electrical properties of epoxy under different frequencies and temperatures. *Journal of Applied Polymer Science*. 140(1). <https://doi.org/10.1002/app.53271>
42. Yao T, Zhang C, Chen K, Niu T, Wang J, Yang Y (2023) Hydroxyl-group decreased dielectric loss coupled with 3D-BN network enhanced high thermal conductivity epoxy composite for high voltage-high frequency conditions. *Composites Science and Technology* 234. <https://doi.org/10.1016/j.compscitech.2023.109934>
43. W. Wang, X. Wang, J. He, Y. Liu, S. Li, Y. Nie (2021) Electric stress and dielectric breakdown characteristics under high-frequency voltages with multi-harmonics in a solid-state transformer. *International Journal of Electrical Power & Energy Systems* 129. <https://doi.org/10.1016/j.ijepes.2021.106861>
44. Huang X, Jiang P, Tanaka T (2011) A review of dielectric polymer composites with high thermal conductivity. *IEEE Electr Insul Mag* 27(4):8–16. <https://doi.org/10.1109/MEI.2011.5954064>
45. Azizi A, Gadinski MR, Li Q, AlSaud MA, Wang J, Wang Y, Wang B, Liu F, Chen LQ, Alem N, Wang Q (2017) High-performance polymers sandwiched with chemical vapor deposited hexagonal boron nitrides as scalable high-temperature dielectric materials. *Adv Mater* 29(35). <https://doi.org/10.1002/adma.201701864>
46. Cheng S, Zhou Y, Li Y, Yuan C, Yang M, Fu J, Hu J, He J, Li Q (2021) Polymer dielectrics sandwiched by medium-dielectric-constant nanoscale deposition layers for high-temperature capacitive energy storage. *Energy Storage Materials*. 42:445–453. <https://doi.org/10.1016/j.ensm.2021.07.018>
47. Burger N, Laachachi A, Ferriol M, Lutz M, Tonazzio V, Ruch D (2016) Review of thermal conductivity in composites: mechanisms, parameters and theory. *Progress in Polymer Science*. 61:1–28. <https://doi.org/10.1016/j.progpolymsci.2016.05.001>
48. Gaal PS, Thermitus MA, Stroe DE (2004) Thermal conductivity measurements using the flash method. *J Therm Anal Calorim* 78(1):185–189. <https://doi.org/10.1023/B:JTAN.0000042166.64587.33>
49. Han Y, Shi X, Wang S, Ruan K, Lu C, Guo Y, Gu J (2021) Nest-like hetero-structured BNNS@SiCnws fillers and significant improvement on thermal conductivities of epoxy composites. *Composites Part B: Engineering* 210. <https://doi.org/10.1016/j.compositesb.2021.108666>
50. Zhang C, Xiang J, Wang S, Yan Z, Cheng Z, Fu H, Li J (2021) Simultaneously enhanced thermal conductivity and breakdown performance of micro/nano-BN co-doped epoxy composites. *Materials*. 14(13):3521. <https://doi.org/10.3390/ma14133521>
51. Blythe AR (1984) Electrical resistivity measurements of polymer materials. *Polymer Testing* 4(2):195–209. [https://doi.org/10.1016/0142-9418\(84\)90012-6](https://doi.org/10.1016/0142-9418(84)90012-6)
52. Wu L, Xiang F, Liu W, Ma R, Wang H (2018) Hot-pressing sintered BN-SiO₂ composite ceramics with excellent thermal conductivity and dielectric properties for high frequency substrate. *Ceram Int* 44(14):16594–16598. <https://doi.org/10.1016/j.ceramint.2018.06.084>
53. Ohba N, Miwa K, Nagasako N, Fukumoto A (2001) First-principles study on structural, dielectric, and dynamical properties for three BN polytypes. *Physical Review B*. 63(11):115207. <https://doi.org/10.1103/PhysRevB.63.115207>
54. Chen J-M, Wang H-P, Feng S-Q, Ma H-P, Deng D-G, Xu S-Q (2011) Effects of CaSiO₃ addition on sintering behavior and microwave dielectric properties of Al₂O₃ ceramics. *Ceram Int* 37(3):989–993. <https://doi.org/10.1016/j.ceramint.2010.11.020>
55. Chen X, Dai C, Hong Z, Awais M, Paramane A, Tanaka Y (2021) Charge dynamics and thermal properties of epoxy based micro and nano hybrid composites at high temperatures. *Journal of Applied Polymer Science*. 138(28):50676. <https://doi.org/10.1002/app.50676>
56. Wang T, Liu C, Li D, Hou Y, Zhang G, Zhang B (2020) Nano ZnO/epoxy coating to promote surface charge dissipation on insulators in DC gas-insulated systems. *IEEE Trans Dielectr Electr Insul* 27(4):1322–1329. <https://doi.org/10.1109/tdei.2020.008793>
57. Wang T-Y, Li X-F, Jie Z, Liu B-X, Zhang G, Liu J-B, Dang Z-M, Wang ZL (2023) Polymer dielectrics with outstanding dielectric characteristics via passivation with oxygen atoms through C-F vacancy carbonylation. *Nano Lett* 23(18):8808–8815. <https://doi.org/10.1021/acs.nanolett.3c01987>
58. Wang P, Min D, Song X, Gao Z, Hao Y, Wang S, Liu W (2023) High temperature energy storage and release properties of polyimide nanocomposites simulated by considering charge trapping effects. *IET Nanodielectrics* 6(3):86–96. <https://doi.org/10.1049/nde.2.12044>
59. Fillery SP, Koerner H, Drummy L, Dunkerley E, Durstock MF, Schmidt DF, Vaia RA (2012) Nanolaminates: increasing dielectric breakdown strength of composites. *ACS Appl Mater Interfaces* 4(3):1388–1396. <https://doi.org/10.1021/am201650g>

60. Bao Z, Hou C, Shen Z, Sun H, Zhang G, Luo Z, Dai Z, Wang C, Chen X, Li L, Yin Y, Shen Y, Li X (2020) Negatively charged nanosheets significantly enhance the energy-storage capability of polymer-based nanocomposites. *Advanced Materials* 32(25). <https://doi.org/10.1002/adma.201907227>

Publisher's Note Springer Nature remains neutral with regard to jurisdictional claims in published maps and institutional affiliations.